



## Impact of Steam-Dilution on the Flame Shape and Coherent Structures in Swirl-Stabilized Combustors

Steffen Terhaar, Kilian Oberleithner & Christian Oliver Paschereit

To cite this article: Steffen Terhaar, Kilian Oberleithner & Christian Oliver Paschereit (2014) Impact of Steam-Dilution on the Flame Shape and Coherent Structures in Swirl-Stabilized Combustors, Combustion Science and Technology, 186:7, 889-911, DOI: [10.1080/00102202.2014.890597](https://doi.org/10.1080/00102202.2014.890597)

To link to this article: <https://doi.org/10.1080/00102202.2014.890597>



Published online: 02 Jun 2014.



Submit your article to this journal [↗](#)



Article views: 435



View related articles [↗](#)



View Crossmark data [↗](#)



Citing articles: 6 View citing articles [↗](#)

## IMPACT OF STEAM-DILUTION ON THE FLAME SHAPE AND COHERENT STRUCTURES IN SWIRL-STABILIZED COMBUSTORS

Steffen Terhaar,<sup>1</sup> Kilian Oberleithner,<sup>2</sup> and Christian Oliver Paschereit<sup>1</sup>

<sup>1</sup>Chair of Fluid Dynamics, Technische Universität Berlin, Berlin, Germany

<sup>2</sup>Laboratory for Turbulence Research in Aerospace & Combustion, Monash University, Clayton, Australia

*Humidified gas turbines and steam-injected gas turbines are promising technologies to lower the emissions and increase the efficiency and fuel flexibility of gas turbines. In the current study, the influence of steam-dilution on swirl-stabilized methane and hydrogen-fired flames is experimentally investigated at Reynolds numbers in the range of 22,000 to 32,000. Velocity fields and flame positions were measured using high-speed particle image velocimetry and OH\* chemiluminescence. An extension of the quantitative light sheet technique was employed to estimate the temperature fields. The combined results reveal strong changes in the flame position, the velocity field, and the temperature field with increasing rates of steam dilution. In particular, three different flow and flame patterns are encountered: At dry conditions, a V-shaped flame stabilizes in a broad inner recirculation zone with low local turbulent kinetic energy; at moderate steam content, the flame changes into a trumpet-like shape; and at very high rates of steam-dilution, the flame detaches and shows an annular shape. The associated coherent flow structures are extracted from the particle image velocimetry data employing proper orthogonal decomposition. The isothermal flow is dominated by a helical instability arising near the combustor inlet. This structure is completely suppressed for the dry flame and reappears for the heavily steam-diluted detached flame with a similar shape and frequency as for the isothermal case. The flow field of the trumpet-like flame at intermediate to high steam dilution rates features a helical instability of lower frequency that is located further downstream than in the isothermal and very wet case. A conceptual explanation is presented that relates the suppression of the helical instability to the specific encountered temperature fields and flame shapes.*

**Keywords:** Coherent structures; Precessing vortex core; Reacting flow field; Steam-dilution; Swirl-stabilized combustor; Temperature estimation

## INTRODUCTION

Using the exhaust heat for steam generation in humidified gas turbines promises high cycle efficiencies at low NO<sub>x</sub> emissions (Bartlett and Westermarck, 2005a, 2005b; Bhargava et al., 2000; Göke and Paschereit, 2013). Compared to combined cycle power generation,

Received 27 August 2013; revised 14 January 2014; accepted 30 January 2014.

Address correspondence to Steffen Terhaar, Technische Universität Berlin, Fachgebiet Experimentelle Strömungsmechanik, Müller-Breslau-Str. 8, Berlin 10623, Germany. E-mail: [steffen.terhaar@tu-berlin.de](mailto:steffen.terhaar@tu-berlin.de)

Color versions of one or more of the figures in the article can be found online at [www.tandfonline.com/gcst](http://www.tandfonline.com/gcst).

steam-diluted gas turbines have the advantage that no steam turbine is required, which reduces plant complexity and installation costs. A key challenge towards the commercial application of heavily steam-diluted gas turbines is the design of a suitable combustor. The effect of dilution, though not necessarily steam dilution, on flame properties of a reactive mixture is a significant reduction of the reactivity and the flame speed (Babkin and V'yun, 1971; Galmiche et al., 2011; Koroll and Mulpuru, 1988; Mazas et al., 2011). While this decreases the risk of flame flashback when operating with high reactivity fuels, such as hydrogen, it also implies challenges for the flame stabilization at high steam-dilution rates.

Nevertheless, Göke et al. (2010) showed that it was possible to achieve a stable flame up to very high steam-dilution rates of more than 30% steam to air mass ratio. They employed the principle of swirl-stabilization, which is used currently in the majority of gas turbine combustors. A strong swirl is imparted on a jet that emanates into the combustion chamber. The centrifugal forces due to the swirl lead to radial and axial pressure gradients and eventually cause a stagnation point near the centerline. This phenomenon is called vortex breakdown and results in large zones of reversed flow and turbulent shear layers between the reversed flow and the jet. Both the recirculation and the high turbulence in the shear layers significantly improve the flame stabilization (Syred and Beér, 1974).

On the other hand, swirling flows undergoing vortex breakdown are prone to the occurrence of self-excited helical flow structures. In particular, a precession of the vortex core around the combustor centerline has been frequently observed (Anacleto et al., 2003; Syred, 2006). This precessing vortex core (PVC) is synchronized with helical Kelvin-Helmholtz instabilities in the shear layers (Oberleithner et al., 2011). In recent years, considerable progress in the understanding of these structures has been made by the application of linear hydrodynamic stability theory (Gallaire et al., 2006; Gallaire and Chomaz, 2003; Oberleithner et al., 2011). The theory explains the self-excited oscillation as a manifestation of a global mode, which is triggered by a region of absolute instability in the flow (Huerre and Monkewitz, 1990; Liang and Maxworthy, 2005).

The effect of combustion on the PVC was reported very ambiguously in a number of studies. In some cases, the instability remained (Froud et al., 1995; Galley et al., 2011; Moeck et al., 2012), was suppressed (Giauque et al., 2005; Roux et al., 2005), enhanced (Syred, 2006), or the suppression depended on the operating conditions (Boxx et al., 2010). The governing mechanisms for the damping of the PVC were suggested to be the increased viscosity (Kuenne et al., 2011; Roux et al., 2005), and low tangential velocities near the centerline (Syred, 2006). Recently, within the authors' group the important role of the density field was shown experimentally (Terhaar and Paschereit, 2012) and analytically (Oberleithner et al., 2013). In the latter, the local stability properties of a hydrodynamically stable attached flame without the incorporation of density effects were calculated, and this virtual isothermal flow was found to be hydrodynamically unstable. When the density effects were incorporated into the analysis, it yielded the suppression of the instability. In the case of a detached flame without significant density gradients along the shear layers, the stability properties are hardly altered by the incorporation of density effects and the flow remained unstable.

The excitation of a PVC can enhance turbulent mixing and the recirculation of hot exhaust gases, thus, affecting the flame stabilization (Galley et al., 2011; Göckeler et al., 2013; Huang and Yang, 2009; Stöhr et al., 2011). Due to the skew symmetric structure of the PVC, no integral heat release fluctuations are caused (Moeck et al., 2012). However, if the mean flow is not completely axisymmetric, analytical models predict integral heat

release fluctuations (Acharya et al., 2013), thus allowing for a coupling with thermoacoustic instabilities.

Thermoacoustic instabilities are caused by a positive feedback loop of integral heat release oscillations and the combustor system acoustics (Lieuwen and Yang, 2005). The influence on the excitation of the PVC is, however, not the only mechanism how different flame shapes (e.g., attached and detached flames) can impact thermoacoustic instabilities. Durox et al. (2009) and Thumuluru and Lieuwen (2009) showed for non-swirling flames and swirling flames, respectively, that different flame geometries resulted in different flame responses to velocity fluctuations. Recently, Hermeth et al. (2013) numerically investigated the transition between a detached and an attached flame state in a swirl-stabilized burner. They confirmed the strong influence of the flame state on the transfer function of velocity to heat release perturbations.

In the present work, we apply optical measurement techniques (high-speed particle image velocimetry (PIV) and OH\* chemiluminescence measurements) to systematically investigate the role of steam-dilution and fuel composition on the flow field and the flame shape. We present an approach to extract planar temperature estimations from the PIV images and employ advanced data analysis techniques (proper orthogonal decomposition) to extract coherent structures from the PIV data. We propose a conceptional explanation that relates the excitation and suppression of the PVC to the specific encountered temperature fields and flame shapes.

The remainder of this study is structured as follows: (1) the experimental approach and the investigated configuration are explained; (2) the mean flow fields and temperature distributions of the (steam-diluted) reacting flows are presented, discussed, and compared to the isothermal flow; (3) the effect of steam-dilution on the coherent structures and the role of the temperature fields are discussed; (4) conclusions of the effect of steam dilution on the flame shapes and the coherent flow structures are drawn.

## EXPERIMENTAL SETUP AND PROCEDURE

### Combustion Test Rig

The experiments were conducted in an atmospheric combustion test rig. The generic burner is presented in Figure 1. Air and steam are premixed before entering the burner at the swirl generator, where fuel is injected through 16 holes arranged in a circle in the bottom plate of the burner. A high degree of mixing is achieved in the annular passage to the combustion chamber. Swirl is imparted to the flow in a movable block swirl generator (Leuckel, 1967) with variable radial and tangential passages. By rotating the lower blocks, the area of the passages and the resulting swirl number can be varied. For the presented results it was adjusted to a fixed theoretical value of  $S = 0.7$ .

The burner outlet diameter  $R = 55\text{mm}$  and the centerbody diameter of 35 mm yield a hydraulic diameter of  $D_h = 20\text{mm}$ . The hydraulic diameter  $D_h$  and the bulk velocity at the burner outlet  $u_0$  are used for normalization throughout this work. A 300-mm-long silica glass tube with an inner diameter of 200mm was used as the combustion chamber. The water-cooled exhaust tube had a length of 750 mm. At the outlet an orifice with a contraction ratio of 8:1 was used in order to suppress self-excited thermoacoustic instabilities. The influence of the orifice on the flow field has been shown to be small for the investigated reacting conditions (Terhaar et al., 2012). However, for reference measurements at isothermal conditions, it had to be removed in order to avoid strong distortions of the flow field.

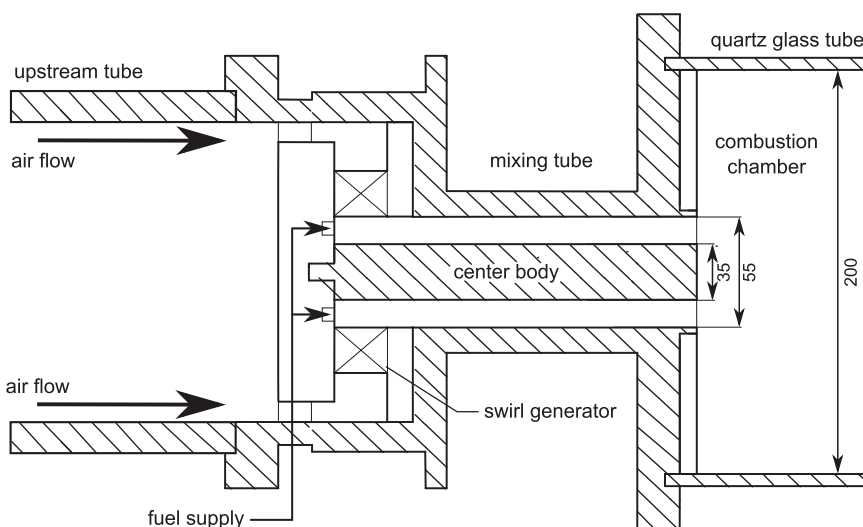


**Figure 1** Schematic of the generic swirl-stabilized burner.

The combustion air was preheated and perfectly mixed with overheated steam upstream of the generic burner. Throughout the study, the steam content  $\Omega$  is described by the steam-to-air mass ratio:

$$\Omega = \frac{\dot{m}_{\text{steam}}}{\dot{m}_{\text{air}}} \quad (1)$$

The total mass flow was kept constant for all measurements at  $\dot{m}_{\text{steam}} + \dot{m}_{\text{air}} = 180 \text{ kg/h}$ , and the steam content was varied between  $\Omega = 0$  and  $0.5$ .

**Table 1** gives an overview of the investigated combustor operating conditions. The inlet temperature  $T_{in}$  as well as the adiabatic flame temperature  $T_{ad}$  were calculated using CANTERA and the GRI 3.0 mechanism (Smith et al., 2000), which was shown to reasonably perform even at high steam-dilution rates (Albin et al., 2013). Subsequently, the temperature of the burnt gases  $T_{fl}$  was estimated using an empirical correlation (Terhaar et al., 2012).

### Velocity and OH\*-Chemiluminescence Measurements

**Figure 2** shows a sketch of the experimental setup for the velocity and OH\*-chemiluminescence measurements in the combustion chamber. An intensified CCD camera

**Table 1** Investigated range of combustor operating conditions

Fuel	$T_{in}$ (K)	$T_{fl}$ (K)	$w_{H_2}$	$\Omega$	$\phi$	Re	$P$ (kW)
Isothermal	620	—	0	0	—	22,500	0
CH <sub>4</sub>	450–620	1620	0	0–0.3	0.6–0.9	22,000–32,000	80–120
CH <sub>4</sub> –H <sub>2</sub>	460–495	1620	0–0.2	0–0.2	0.56	25,400–289,000	84–88
H <sub>2</sub>	450–620	1436–1620	100	0.2–0.5	0.6–0.9	24,100–32,000	56–84

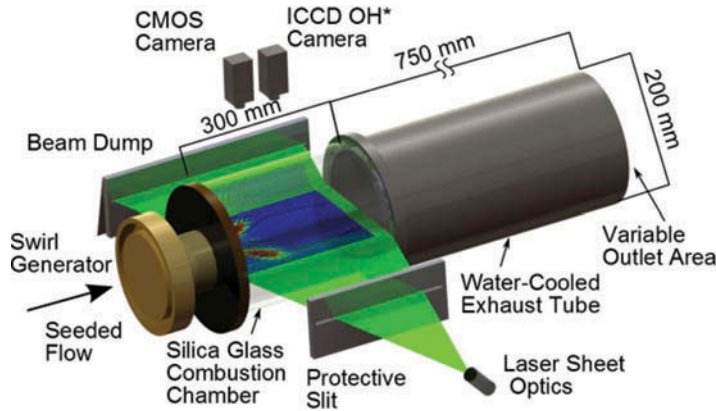


Figure 2 Sketch of the experimental setup.

with an 85 mm  $f/3.5$  UV lens and a band pass filter centered at 308 nm was used to give the spatial distribution of  $\text{OH}^*$  chemiluminescence. In the case of a perfectly premixed fuel-air mixture, the  $\text{OH}^*$ -chemiluminescence intensity correlates with the heat release rate and the intensity of the chemical reaction (Higgins et al., 2001). However, also for technically premixed cases, as in the present study, it is often taken as a qualitative indicator of the flame position.

Flow velocities were measured using high-speed PIV at a horizontal plane containing the combustor axis. The PIV system consisted of a dual cavity diode pumped ND:YLF laser and a high-speed CMOS camera equipped with a 135 mm  $f/2.0$  lens. The camera is able to operate in full frame mode ( $1024\text{px} \times 1024\text{px}$ ) up to 5400 fps. In double frame mode this resulted in a recording speed of 2.7 kHz of the PIV system. A light sheet optic formed a laser sheet with a thickness of 1 mm and the beam waist located slightly beyond the measurement area.

The time delay between the pulses was set according to the expected flow velocities between 12 and 16  $\mu\text{s}$ . The strong out-of-plane velocity component associated with swirling flows required a rather short pulse separation in order to minimize lost particle pairs. Titanium dioxide ( $\text{TiO}_2$ ) particles of a nominal diameter of 1  $\mu\text{m}$  were seeded into the flow upstream of the swirl generator using a brush-based powder disperser to ensure a very homogeneous particle distribution. Reflections of the incoming laser light from the silica glass were minimized by using beam dumps for the sheet and primary reflections. Further reflections could be eliminated by sandblasting parts of the silica glass. The steam led to corrosion of the glass, which had to be replaced regularly.

The images were post-processed with a final interrogation area of  $16\text{px} \times 16\text{px}$ . The interrogation window overlap of 50% resulted in a spatial resolution of 3.6 and a vector spacing of 1.8 mm. The data was filtered for outliers (typically less than 3%) and interpolated from adjacent interrogation areas. Based on the uncertainty of the correlation peak-finding algorithm of 0.1 px, the random uncertainty of the instantaneous velocities is estimated as 1.2 to 1.6 m/s, depending on the pulse separation. This error, which is approximately 2% of the bulk velocity, contributes mostly to the root mean square (RMS) error.

### Proper Orthogonal Decomposition

The extraction of coherent structures from the flow field measurements is achieved by the application of proper orthogonal decomposition (POD), which is a well-established technique in fluid mechanics (Berkooz et al., 1993). It is carried out by projecting  $N$  PIV snapshots onto an orthogonal  $N$ -dimensional vector base that maximizes the turbulent kinetic energy content for any subset of the base. In other words, the POD modes provide a least-order expansion of the fluctuating flow field, such as

$$v'(x, t) = \sum_{j=1}^N a_j(t) \Phi_j(x) + v_{res}(x, t) \quad (2)$$

by minimizing the residual  $v_{res}$ . The  $a_j(t)$  are called temporal POD coefficients, while  $\Phi_j(x)$  are the spatial POD modes or simply POD modes. The amount of the fluctuating kinetic energy contained in each POD mode is given by

$$K_j = \overline{\langle v', \Phi_j \rangle^2} / 2 = a_j^2 / 2 \quad (3)$$

with  $\langle u, v \rangle$  being the inner product of the vectors  $u$  and  $v$ . This system reduction strategy allows for an accurate description of turbulence data using only a limited number of modes. Furthermore, when applied to time-resolved data, the temporal POD coefficients  $a_j(t)$  can be used to investigate the temporal behavior of the corresponding POD mode.

The POD approach provides an orthogonal set of spatial and temporal modes that are energy ranked. The spatial modes provide the shape of the coherent structure, while the Fourier spectra of the temporal modes readily reveal any dominant frequencies related to these modes.

Note that the orthogonalization of the POD procedure is not physical and POD modes cannot be rigorously associated with coherent structures. It may occur that a dominant dynamical feature is spread over several POD modes. However, as can be observed later in this study, the flow instabilities always manifest themselves in a strong single-tone limit-cycle oscillation, which can be clearly associated with a pair of similarly strong POD modes of a similar spatial shape and whose time coefficients peak at the same oscillation frequency. Thus, for the investigated cases the POD provides a convenient tool to extract coherent structures from the turbulent flow field (Oberleithner et al., 2011).

### Temperature Estimation

Distributions of the density and temperature field inside the combustor were estimated using the quantitative light sheet (QLS) technique. The QLS technique is mainly used as an alternative to laser induced fluorescence (LIF) measurements for mixing experiments, where the flow is only partly seeded (Findeisen et al. 2005; Roehle et al. 2000; Voigt et al., 1997). However, the principle is transferrable to density measurements in a homogeneously seeded flow. The big advantage of the QLS technique is the simplicity of the setup compared to Rayleigh or Raman scattering based techniques. The experimental



setup is almost identical to the PIV setup, what makes the QLS technique very suitable to be used simultaneously to PIV measurements.

In the QLS technique, the amount of scattered light is used to derive the spatial distribution of the seeding density, which can be correlated to either mixture fractions at non-premixed conditions or the fluid density at premixed conditions. The recorded intensity signal does not only depend on the seeding particle density but also on several other factors. However, the most important parameters can be described by a simplified model (Findeisen et al., 2005; Freund et al., 2011):

$$I(x, y) = P(x, y) IL(x, y) K(x, y) + H(x, y) + D(x, y) \quad (4)$$

In this model the measured intensity of the scattered light ( $I$ ) consists of three parts. The first term represents the light intensity scattered by the seeding particles. It depends on the distribution of the particle density ( $P$ ), on the local light sheet intensity ( $IL$ ), and on a factor ( $K$ ) that accounts for different viewing angles in the measurement plane. For details see Findeisen et al. (2005) and Freund et al. (2011). The second term stems from reflections of the light at the silica glass combustion chamber ( $H$ ), and the last term ( $D$ ) represents the camera dark current. Other physical effects, such as light extinction, multiple scattering, and illumination of the background due to seeding, are assumed to be of secondary importance (Freund et al., 2011) and are neglected in this simple model and in the scope of this study.

In order to correct for the background light and dark current ( $H$  and  $D$ ), reference pictures ( $I_0$ ) without seeding ( $P = 0$ ) were recorded and subtracted from the raw images:

$$I_0(x, y) = H(x, y) + D(x, y) \quad (5)$$

For the correction of the local light sheet intensity ( $IL$ ) and the viewing angle ( $K$ ), images at isothermal conditions and, hence, an almost homogeneous particle density distribution ( $P_h$ ) were recorded:

$$I_h(x, y) = P_h IL(x, y) K(x, y) + D(x, y) + H(x, y) \quad (6)$$

With the known homogeneous particle density  $P_h$ , the particle density distribution  $P$  for a measured light intensity distribution ( $I$ ) can be obtained:

$$P(x, y) / P_h = (I(x, y) - I_0(x, y)) / (I_h(x, y) - I_0(x, y)) \quad (7)$$

In order to convert particle density distributions into fluid density distributions, it must be assumed that the scattering cross section of the particles does not change inside the measurement plane and that the velocity field does not cause changes in the particle density.

The melting temperature for the  $\text{TiO}_2$  seeding is higher than any temperatures reached in the combustor. Hence, it can be assured that the size distribution of the particles does not change due to heat release. Changes in the seeding density inside of smaller eddies could be observed to a limited extent, even in the homogeneously seeded isothermal case. This is assumed to stem from the higher density of  $\text{TiO}_2$  compared to air. Particles are transported out of the core of the eddy due to centrifugal forces. However, these inhomogeneities disappear in the averaged raw image. Thus, only averaged density and temperature fields can be



extracted with the proposed technique. Inhomogeneities in the mean seeding density distribution caused by the swirling motion of the flow are accounted for in Eq. (6), as they also occur when measuring  $I_h$ . However, this correction only provides a first order correction as it assumes similar tangential velocities under isothermal and reacting conditions.

Due to the fact that several parameters determine the total amount of scattered light, the QLS technique is commonly used as a relative technique only. This means that a reference density is necessary to deduce absolute values from the measurements. From Eq. (6), it follows that the density distribution can be obtained if the density distribution  $\rho_h$  of the homogeneous image  $I_h$  is known and it is assumed that the particle density is proportional to the fluid density:

$$\rho(x, y) = \rho_h P(x, y) / P_h \quad (8)$$

From the density distribution, the temperature distribution can be readily derived if ideal gas behavior and negligible pressure drop over the flame are assumed.

$$\tilde{T}(x, y) = T_h(x, y) \frac{\rho_h}{\rho(x, y)} \quad (9)$$

A comparison with point-wise measured temperature data obtained using a precise suction pyrometer (Göke and Paschereit, 2013) showed that the absolute values of  $\tilde{T}$  differed up to 20% from the suction pyrometer data, although the shape of the temperature field was reproduced very well. This is assumed to stem from long-term variations of the seeding intensity, which directly influences the measured light intensity and cannot be corrected for. If the temperature data is scaled with the estimated temperature of the burned gases (Terhaar et al. 2012), a very good agreement of the temperature data from the QLS technique to the point wise measured data is achieved, as can be observed in Figure 3. In other words, the proposed temperature estimation employing the QLS technique provides a very convenient way to obtain qualitative temperature distributions of reacting

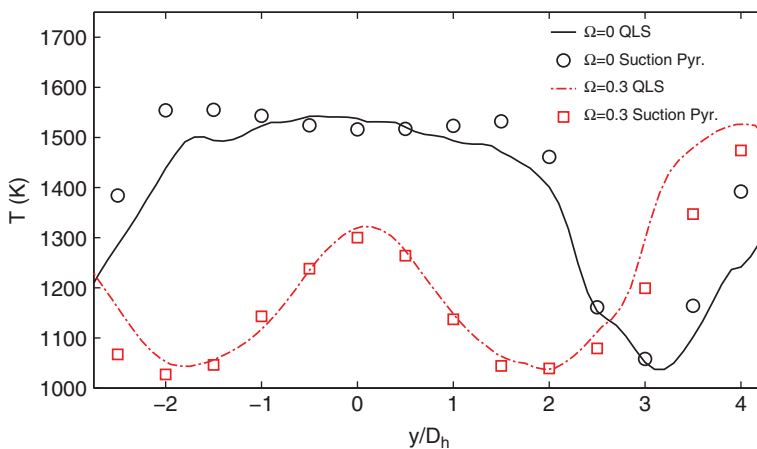


**Figure 3** Comparison of estimated temperature profiles (lines) to measured data (circles) at  $x/D_h = 5$  for two different operating conditions. (Source: Göke and Paschereit, 2013.)

flows. If point wise temperature data are available, a reasonable quantitative estimation is possible.

## RESULTS AND DISCUSSION

### Flow Field and Flame Shape

Before the effect of combustion on the flow field is described, the flow field topology of the isothermal case, which serves as a reference, is presented in [Figure 4](#). Streamlines of the two dimensional velocity vectors measured on radial-axial planes are superimposed on the normalized turbulence intensity. Additionally, radial profiles of the axial velocity component are extracted at various axial locations. Four regions can be identified: An annular jet emanating from the mixing tube, an internal recirculation zone (IRZ) generated by vortex breakdown, an outer recirculation zone (ORZ) induced by the area change and the confinement, and a comparably small recirculation resembling the centerbody wake. In between the jet and the large recirculation regions, turbulent shear layers are produced, with very high levels of turbulence.

These basic features of the isothermal flow field (jet, IRZ, ORZ, and wake) are also encountered for the reacting cases considered. However, it is observed that the combustion significantly alters the opening angle of the jet. To quantify this effect, the local opening angle  $\alpha_x$  is defined as:

$$\alpha_x(x) = \text{atan} \left( \frac{dr_p(x)}{dx} \right) \quad (10)$$

where  $r_p(x)$  is the radial position of the peak axial velocity. Subsequently, the initial opening angle  $\alpha$  of the emanating jet is defined as the average of  $\alpha_x$  from  $\frac{x}{D_h} = 0.5$  to 4.

[Figure 5](#) shows the measured jet opening angle over the calculated axial center of gravity of the flame  $x_{fl}$  for the complete range of operating conditions. The axial center of gravity of the flame is defined as:

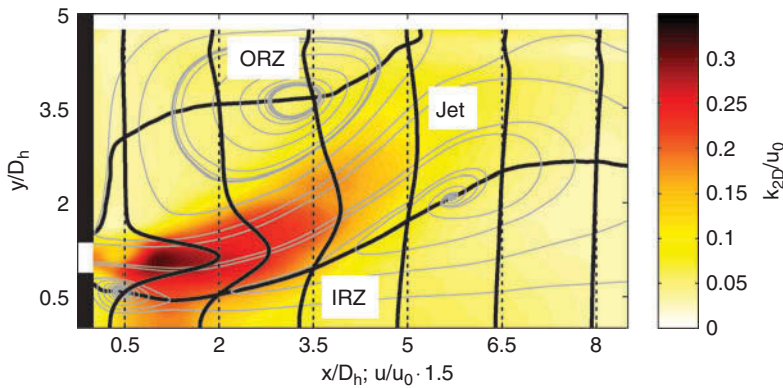


**Figure 4** Topology of the isothermal flow field at dry conditions. Streamlines are superimposed on the normalized turbulent kinetic energy. Thick black solid lines show radial velocity profiles of the axial velocity component. Thick black dashed lines are isolines of zero axial velocity.

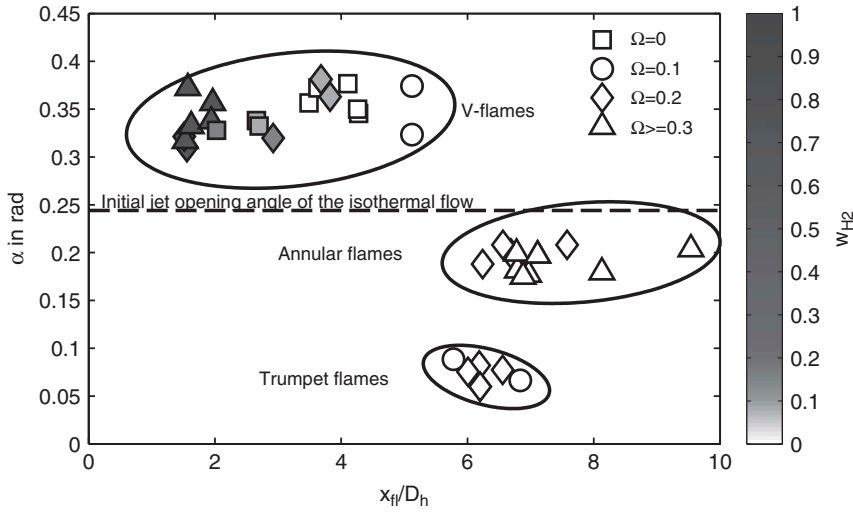


**Figure 5** Initial jet opening angle over axial location of the flame for various operating conditions. The shape of the markers indicates the rate of steam-dilution and the color of the mass fraction of hydrogen in the fuel.

$$x_{fl} = \frac{\int I_{OH}(x, r) x dV}{\int dV} \quad (11)$$

where  $I_{OH}(x, r)$  denotes the Abel deconvoluted  $OH^*$ -chemiluminescence intensity distribution.

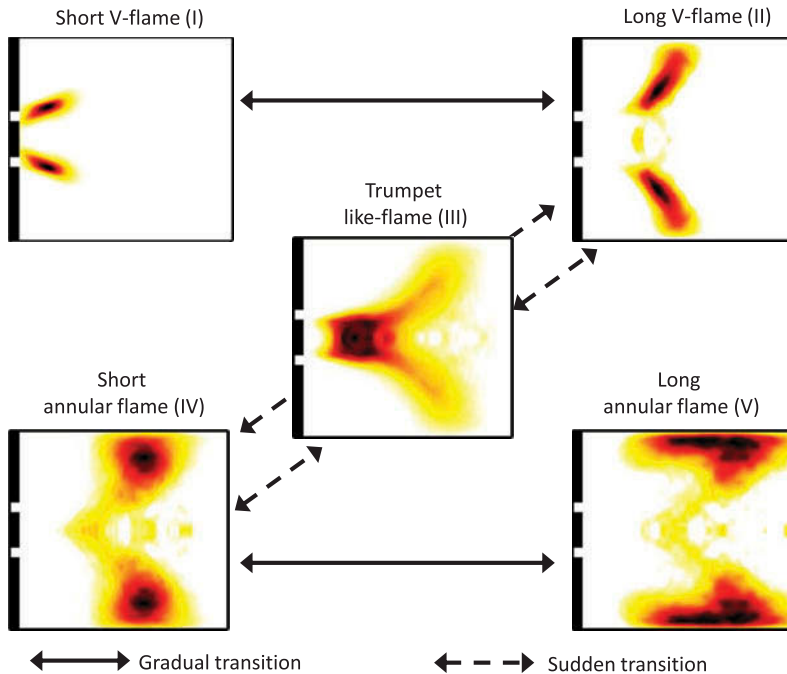
Three regions can be distinguished in Figure 5. The first region represents flames that are anchored near the combustor inlet with a very wide jet opening angle (V-flames), the second regions comprises flames that are located further downstream with slightly smaller jet opening angles than for the isothermal case (annular flames), and another region resembles very small jet opening angles with flames at intermediate locations (trumpet-like flames).

From Figure 5 a clear correlation of the axial location of the flame to the flow field type can be observed. Furthermore, it is evident that steam dilution causes the flame to move downstream while hydrogen enrichment has an opposite effect. However, the large number of free parameters (inlet temperature, fuel composition, steam-dilution rate, and equivalence ratio) makes any direct investigation of the influence of single parameters very difficult. To avoid this problem, a second set of operating conditions is investigated, where two important parameters have been kept constant. The inlet temperature was kept at 620 K and the equivalence ratio was adjusted to achieve a constant flame temperature of 1620 K while changing the fuel composition or the rate of steam dilution. The selected operating conditions, which cover all encountered regions of Figure 5, are summarized in Table 2.

Figure 6 shows the flame shapes and the possible transitions for the selected operating conditions. The top left flame (I), encountered for hydrogen, is the most compact V-flame. If the amount of hydrogen is reduced, the flame becomes continuously longer, but it remains anchored at the center body and exhibits a V-shape (II). When steam-diluting the flame,

**Table 2** Combustor operating conditions for the different flame shapes depicted in Figure 6

Flame shape	No.	$T_{in}$ (K)	$T_{ad}$ (K)	$T_{fl}$ (K)	$w_{H_2}$	$\Omega$	$\phi$	Re	$P$ (kW)
Isothermal	(–)	620	—	—	0	0	—	22,500	0
Short V	(I)	620	1850	1620	100	0.3	0.75	25,200	101
Long V	(II)	620	1850	1620	0	0	0.56	23,700	81.4
Trumpet-like	(III)	620	1850	1620	0	0.1	0.68	24,600	89.9
Short annular	(IV)	620	1850	1620	0	0.2	0.8	25,400	96.9
Long annular	(V)	620	1850	1620	0	0.3	0.92	26,000	102.9

**Figure 6** Overview of the encountered flame shapes for combustion of methane and hydrogen with increasing rates of steam dilution. The Abel deconvoluted OH\*-chemiluminescence intensity is color coded.

the flame first becomes longer. At a certain amount of steam ( $\Omega \sim 0.1 - 0.2$ ), the flame anchors in the wake of the center body and abruptly changes into a very long, trumpet-like flame (III). A further increase of the rate of steam dilution (typically  $\Omega = 0.2$  to  $0.3$ ) leads to detached flames located further downstream in the combustion chamber that show an annular shape (IV). The abrupt transition to the detached flame can either take place from the trumpet-like flame (III) or directly from the V-flame (II). Starting from the annular flame (IV), an increase of the rate of steam dilution leads to an increasingly distributed annular flame located even more downstream (V).

When the methane fuel is enriched by hydrogen, the transition from the V-flame to the trumpet-like flame or the annular flame occurs at considerably higher rates of steam dilution. On the other hand, parameters that lower the reactivity of the mixtures, such as lower inlet temperatures or leaner mixtures, cause transitions at lower rates of steam dilution or even dry conditions.

### Flow Characteristics Encountered at Different Flame Shapes

A detailed investigation of the flow field, the temperature field, and the turbulence characteristics is carried out in the following for three flow field and flame types (II, III, IV). The results for the short V-flame (I) and the long annular flame (V) are very similar to the results for the long V-flame (II) and the short annular flame (IV), respectively, and are omitted here due to space limitations.

Radial profiles of the axial velocity, the turbulent kinetic energy, and the estimated temperatures are presented in Figure 7 for the three selected operating conditions that represent the three encountered flame and flow field shapes. For the sake of comparison, the isothermal velocity profiles are repeated in all graphs. All velocity fields show the same basic features as the isothermal flow field presented in Figure 4. The jet and the recirculation zones with negative axial velocities can be clearly observed. However, some major differences between the flow fields are present and will be described in the following.

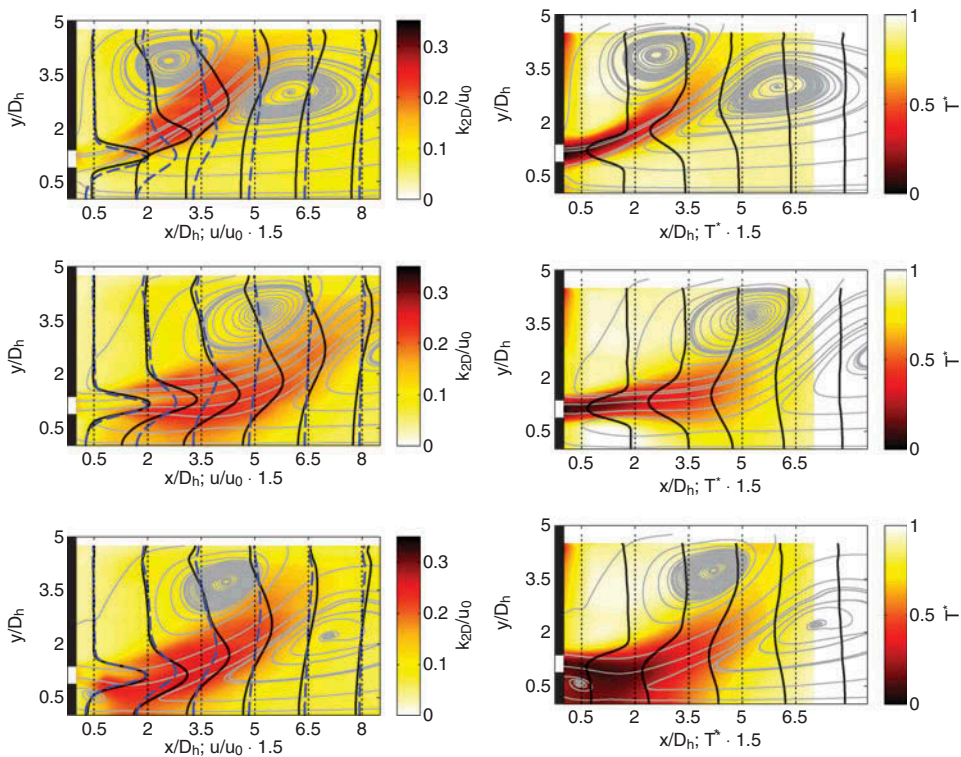


**Figure 7** Measurement results at increasing rates of steam dilution (top to bottom). Left column: Radial profiles (black lines) of the mean axial velocity component superimposed on contours showing the normalized turbulence intensities. Streamlines of the mean axial and radial velocity components are also shown indicating the IRZ and the ORZ. Blue dashed lines represent radial profiles of the mean axial velocity component of the isothermal case. Right column: Radial profiles of the normalized temperature superimposed on contours showing the normalized temperature. Low temperature regions in the ORZ are measurement artefacts due to reflections of the laser sheet at the combustor plate.

The velocity profiles of the V-shaped flame, which anchors in inner shear layers, differ significantly from the isothermal flow field. Already near the combustor inlet, the location of the peak of the axial velocity is considerably shifted to higher radii. The velocities in the jet are higher, whereas the magnitudes of the back-flow velocities near the combustor inlet are lower. Similarly to the isothermal flow field, the strongest turbulent fluctuations occur in the inner shear layer between the jet and the inner recirculation zone (IRZ). However, the amount of turbulence is considerably lower than for the isothermal case. Particularly in the inner recirculation zone, where the back-flow velocities are uniform for the V-flame, the turbulence intensities are very low. The normalized temperature distribution of the V-flame shows that the IRZ and the ORZ of the V-flame are completely filled with hot reaction products. The temperature gradients are very high, due to the relatively low turbulence levels.

The velocity profiles of the trumpet-like flame show a very narrow IRZ and a small opening angle of the jet. Compared to the isothermal case, the back-flow velocities are considerably higher. The turbulence intensities near the combustor inlet are higher than for the V-flame, but lower than in the isothermal case. However, the axial decay of the turbulence is slower, leading to higher turbulence intensities at the more downstream positions. Similarly to the V-flame, the IRZ and ORZ of the trumpet-like flame are filled with hot combustion products. Downstream of  $\frac{x}{D_h} = 2$ , the temperature gradients are considerably smoothed out. This is caused by the higher turbulence intensities.

When the flame is no longer able to anchor in the wake of the center body and in the inner shear layer, the flame detaches and shows an annular shape. This resulting flow field is very similar to the isothermal flow field with a slightly smaller opening angle of the jet and higher velocities due to dilatation. The turbulence distribution shows the highest levels in the jet and the IRZ. This causes the rapid mixing of hot combustion gases recirculating from the flame region with the cold jet of fresh gasses. As a consequence, almost no radial gradient of the temperature is present along the inner shear layer. The presence of the cold gasses in the IRZ and high local strain rates seem to effectively inhibit a reattachment of the flame into the V-shape or the trumpet-like shape. Consistently, in the experiments a hysteresis for the transition from the detached to the attached flames was observed.

### Coherent Structures Encountered at Different Flame Shapes

The flow field and density measurements showed a significant influence of the turbulence intensities on the temperature distributions. Furthermore, a recent study employing tracer experiments (Göckeler et al., 2013) suggests that coherent structures play an important role for the considerably increased mixing in the case of the detached flame. Isothermal swirling jets undergoing vortex breakdown are typically dominated by single-helical coherent structures (Liang and Maxworthy, 2005; Oberleithner et al., 2011; Ruith et al., 2003). The same instability, also known as a precessing vortex core, is found to arise in the presently investigated combustor flows. In the following, we employ proper orthogonal decomposition (POD) in order to extract the dominant dynamics from the time-resolved flow measurements. For each operating condition, an ensemble of 3000 samples is considered.

Before assessing the occurrence of the coherent structures in the different flame configurations, the outcome of the POD analysis at isothermal conditions, where a PVC is present, is described. Figure 8a shows the energy distribution  $K_j$ , the normalized power spectral density (PSD) of the POD coefficients  $a_i(t)$ , and the corresponding time traces.

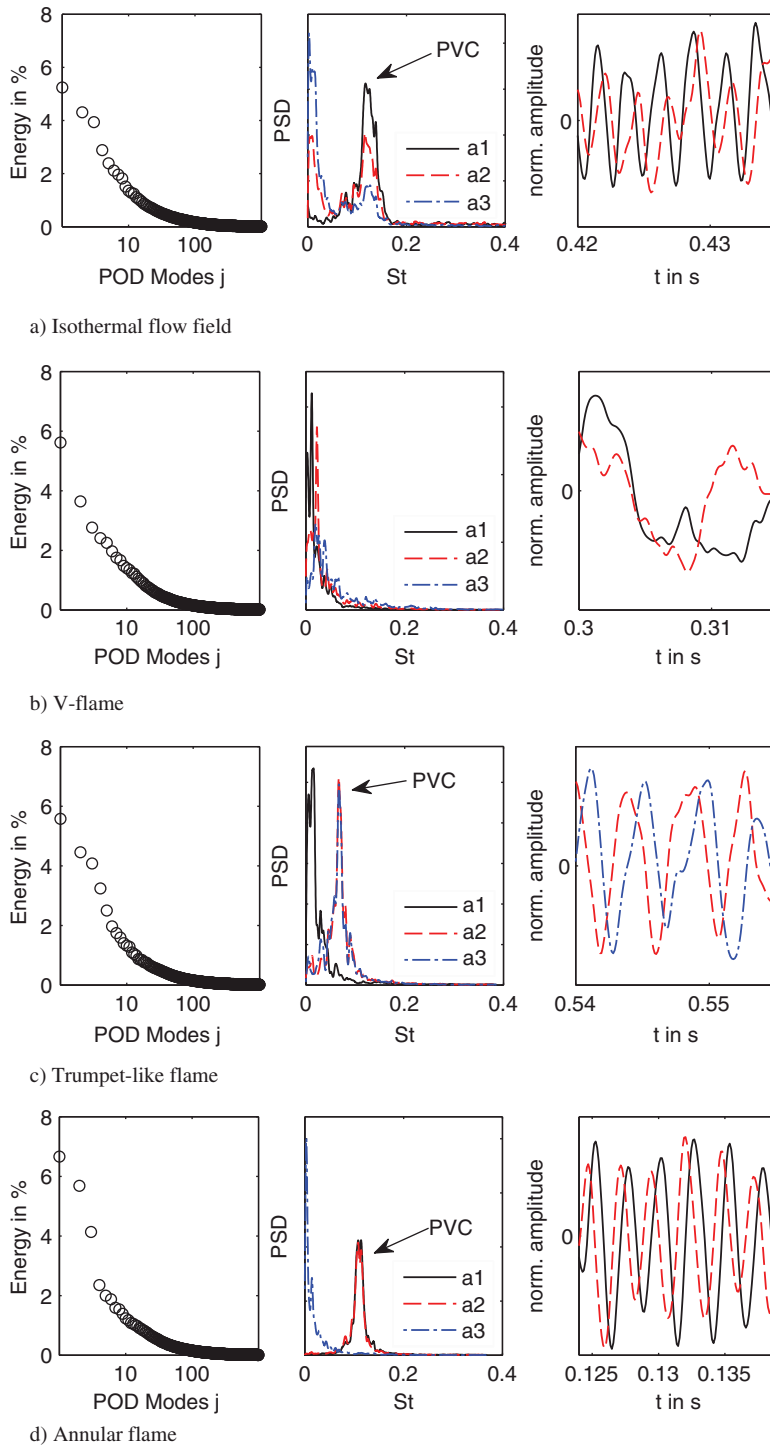


**Figure 8** Results of the POD analysis. (a) Isothermal case, (b) V-flame ( $\Omega = 0$ ), (c) trumpet-like flame ( $\Omega = 0.1$ ), and (d) annular flame ( $\Omega = 0.2$ ). First column: Modal energy distribution  $K_j$  in percent. Second column: Normalized power spectral density (PSD) of the POD coefficients  $a_i(t)$  of the three most energetic modes. Third column: Time traces of the most energetic temporal coefficients.



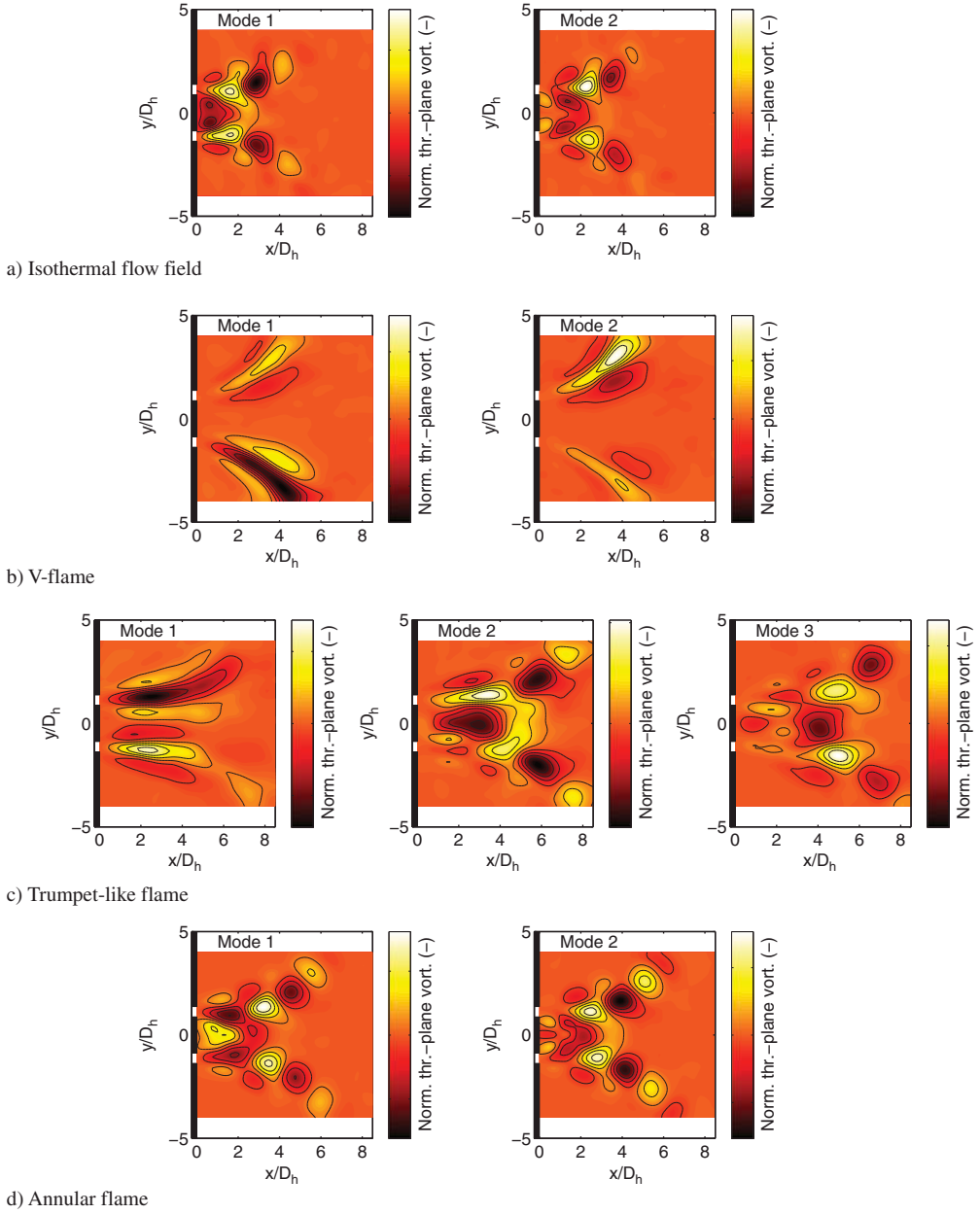


**Figure 9** Normalized through-plane vorticity of the most energetic POD modes. PVC is clearly visible for the isothermal case (a) and the annular flame (d). PVC is shifted downstream for the trumpet-like flame (c), and suppressed for the V-flame (b).

It can be observed that around 10% of the fluctuating kinetic energy is captured by the first two modes. The spectra of these two modes reveal a distinct peak at around  $St = 0.11$  and the corresponding time traces show that the first two modes oscillate in time at a phase shift of a quarter period. Consistently, the first two spatial POD modes (Figure 9a)

span a convective vortex pattern that is very typical for isothermal swirling jets. It is associated with a self-excited single-helical instability that features a precessing vortex core (PVC) (Oberleithner et al., 2011; Stöhr et al., 2011). Analogously to a traveling sine wave expressed by a superposition of a sine and cosine, the global flow oscillations encountered here can be expressed by the two most energetic POD modes.

Ideally, the spectral peaks of the first modes, shown in Figure 8, should be discrete and equally high. The encountered broadening of the peak is associated with jitter in the phase and in the spatial structure due to turbulence. The difference in height is associated with the spatial truncation of the POD modes and has no physical meaning. Nonetheless, by referring to previous findings, the POD is sufficiently clear to conclude that the isothermal flow features a helical coherent structure at a Strouhal number of 0.11.

For the V-flame (Figure 8b), the spectra do not reveal any prominent peaks except for low frequency contributions that are associated with long time flow variations. The spatial shape of these modes (Figure 9b) reveals that these modes describe a slow axisymmetric longitudinal (mode 1) and asymmetric lateral movement (mode 2) of the shear layers. The low frequency content of these modes indicates that these dynamics are not related to shear instability, and one may conclude that this configuration is not unstable to the PVC mode.

The spectra of the trumpet-like flame (Figure 8c) show a very slow oscillation for the first mode. The spatial shape of this mode is similar to the second mode of the POD of the V-flame. Consequently, this mode describes a slow asymmetric lateral movement of the shear layers. Additionally, a distinct peak for the 2nd and 3rd mode at a frequency ( $St = 0.06$ ) that is somewhat lower than the instability frequency for the isothermal case but clearly above the frequency of the first mode is evident in Figure 8c. These two modes capture around 10% of the fluctuating kinetic energy and represent a dynamical feature that is similar to the isothermal flow, indicating that the reacting flow at this operating condition is subjected to a strong flow instability that manifests in a PVC. The spatial POD modes (Figure 9c) reveal that for the reacting flow field of the trumpet-like flame, the coherent flow pattern in the inner shear layer is significantly shifted downstream compared to the isothermal case.

The POD analysis of the annular flame configuration (Figure 8d) shows a strong helical instability that is surprisingly similar to the isothermal case. The spectra of the two most energetic POD modes, which account for 12% of the fluctuating kinetic energy, peak clearly at the same frequency ( $St = 0.11$ ) as in the isothermal case. The spatial POD modes (Figure 9d) reveal stronger vertical structures and slower streamwise decay. For these operating conditions, the helical instability and associated coherent structures are not suppressed by the combustion but they are considerably amplified and show less frequency jitter, which is in contrast to previous observations (Roux et al., 2005).

### The Role of the Temperature Field

The coherent structures found at isothermal conditions, for the annular flame, and for the trumpet-like flame can be attributed to self-excited global flow oscillations. These oscillations correspond to a so-called global mode triggered by an inherent flow resonance (Gallaire et al., 2006; Liang and Maxworthy, 2005; Oberleithner et al., 2011, 2012). A necessary condition for the resonance is a sufficiently large region of absolutely unstable flow (Huerre and Monkewitz, 1990), where perturbations can grow in downstream and upstream direction. In contrast to that, in a convectively unstable flow, the perturbations grow in downstream direction only.

In an isothermal flow, the growth rate of a convective instability scales with the inverse of the shear layer thickness (Michalke, 1965). The growth rate of an absolute instability, on the other hand, depends on both the shear layer thickness and the back flow intensity. Qualitatively speaking, the first determines the growth rate and the second the convective velocity. Thus, a sufficiently large region of back flow with strong shear is required for a global flow oscillation to arise.

In the case of non-isothermal flows, the temperature/density field generally has a significant influence on the perturbation growth rates and consequently on the absolute instability. As shown by Monkewitz and Sohn (1988), a hot (low density) jet emanating in cold (high density) fluid is destabilized due to the density stratification. Based on linear stability analysis, they conclude that a flow with co-signed gradients of the velocity and temperature profiles shows higher absolute growth rates than an isothermal flow. This dependency is illustrated in Figure 11. Consequently, the cold jet of unburned gas entering the combustion chamber is stabilized when it penetrates into regions of hot burned gases. This explains why the V-flame configuration, which is characterized by a cold jet at the combustor inlet that penetrates a large IRZ that is completely filled with hot burned gasses, reveals no global helical instability. The strong temperature stratification in the inner shear layers encountered in this configuration causes the suppression of the helical instability.

A similar density field is encountered in the trumpet-like flame near the nozzle. However, in this case, the inner axial shear layer spreads less rapidly with downstream distance and the recirculating velocities are considerably higher. This may explain the occurrence of the helical instability for the trumpet-like flame at a further downstream location, where the temperature gradients are less pronounced. In the case of the annular flame, the temperature is almost constant across the inner shear layer. Hence, the helical instability is not influenced by the temperature field, and therefore, the resulting instability remains similar in shape and frequency to the isothermal case. This is also evident in Figure 10, where the measured normalized frequencies of the coherent structures at various operating conditions including a wide range of Reynolds numbers and equivalence ratios are presented. The frequencies are almost constant for the annular flames and equal to the isothermal frequencies. A slight dependence on the temperature ratio is evident for the trumpet-like flames. As explained above, the instability in the case of the trumpet-like flames depends on the combination of flame length, shear layer thickness, back flow

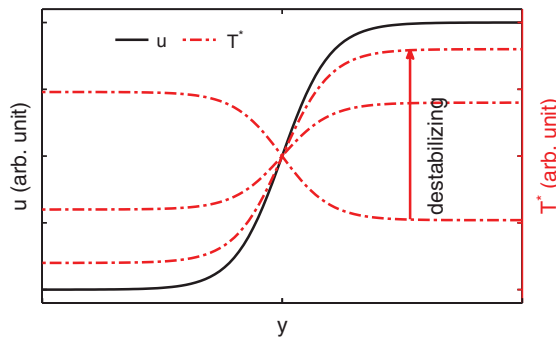


**Figure 10** Schematic visualization of the stabilizing or destabilizing effect of temperature stratification. Gradients in the same direction destabilize the shear layer and gradients in the opposite direction stabilize the shear layer.

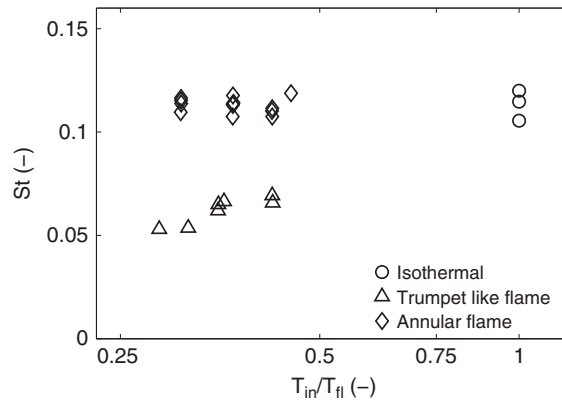


**Figure 11** Frequency of the self-excited flow instability taken from PIV data and expressed as a non-dimensional Strouhal number. Frequency slightly increases with the temperature ratio for the trumpet-like flame and is constant for the isothermal case and the annular flame.

intensities. All three parameters, and in particular the flame length, are affected by the operating conditions, possibly causing the changes in the oscillation frequency.

As described above, the temperature and density field is an important parameter for the occurrence of the helical instability. However, also the helical instability may significantly influence the temperature distribution. In Figure 7, it is evident that the turbulence intensities are higher in the regions where a helical instability resides. Moreover, the large-scale coherent structures considerably increase the mixing between the jet and the IRZ (Göckeler et al., 2013), smoothing out the radial temperature gradients along the shear layer. In the case of the detached flame, this effectively inhibits a reattachment of the flame. As a result, a hysteresis is encountered between the detached and the attached flames.

## CONCLUSIONS

The flow field and flame characteristics of a swirl-stabilized combustor operating on methane and hydrogen fuel were investigated under dry and steam-diluted conditions using PIV and  $\text{OH}^*$  chemiluminescence imaging. To estimate the density field and temperature field, the QLS technique has been extended and validated. The dominant coherent flow structures were encountered at different flow configurations where extracted from the turbulent flow measurements by means of POD.

Three types of flame shapes and corresponding flow and temperature fields were found depending on the operating conditions. Both the mean flow field and turbulence characteristics depend significantly on the flame shapes.

- Dry flames and steam diluted hydrogen or hydrogen enriched flames exhibited a V-shape. The flow fields showed high negative velocities in the IRZ and a wide jet opening angle, resulting in a broad IRZ. The turbulence intensity near the burner outlet was significantly reduced compared to the isothermal flow. In particular, inside the IRZ very low turbulence levels were measured.

- A trumpet-like flame was found at intermediate steam levels. The flow field as well as the flame showed a particular form with a very narrow IRZ with combustion along the inner shear layer.
- At high steam dilution rates the flames detached and showed annular shapes located in a broad range of axial positions further downstream than for the other flame shapes. The flow fields of the annular flames showed a good agreement with the isothermal flow. The shape of the velocity and turbulence profiles remained nearly unaltered near the burner outlet. Further downstream, flow velocities were higher due to heat release and the IRZ became slightly narrower. Turbulence profiles scaled similar as the velocity profiles.

At isothermal conditions, a helical flow instability that manifested in a PVC was found. This coherent structure was completely suppressed for the V-flames. The trumpet-like flame at moderate steam levels ( $\Omega = 0.1 - 0.2$ ) featured a helical coherent structure that was located further downstream and precessed at a lower frequency than for the isothermal case. The flow fields of the annular flames at high levels of steam dilution ( $\Omega \geq 0.2$ ) showed coherent structures that were very similar to the isothermal case in appearance and frequency.

The results of this study show how the operating conditions, in particular the steam dilution rate, induce different flow fields and flame shapes, which are of high relevance for gas turbine operation, as they directly influence the stability of the combustor. Furthermore, the presented work describes how the flame shapes are related to the occurrence of the PVC. It is suggested that the suppression or modification of the helical instability driving the PVC mainly stems from the radial temperature gradient across the inner shear layers. If the PVC is excited, it tends to smooth out the temperature gradients, cool down the inner recirculation zone, and inhibit a reattachment of the flame. Moreover, the results of this study allow for the prediction of the occurrence and shape of the PVC from a prediction of the flame shape.

## ACKNOWLEDGMENTS

The authors would like to thank Andy Göhrs, Eduard Höschele, and the CONFET for assistance in the lab and helpful discussions.

## FUNDING

The research leading to these results has received funding from the European Research Council under the ERC grant agreement no. 247322, GREENEST and was supported by a fellowship within the Postdoc-Program of the German Academic Exchange Service (DAAD).

## NOMENCLATURE

$a_j$	temporal coefficient of POD mode $j$
$D_h$	hydraulic diameter (m)

$D$	camera dark current
$H$	camera current due to reflections
$I$	camera current
$IL$	local light sheet intensity
$I_h$	current with homogeneous particle distribution
$I_0$	reference current
$I_{OH}$	OH* chemiluminescence intensity
$K$	correction factor
$K_j$	kinetic energy of POD mode $j$
$k_{2D}$	two-dimensional turbulence intensity
$\dot{m}_{\text{steam}} + \dot{m}_{\text{air}}$	air and steam mass flow (kg/s)
$P$	combustor power (kW)
$P$	particle density
$P_h$	homogeneous particle distribution
$R$	combustor inlet radius (m)
Re	Reynolds number
$r_p$	radial location of the maximum axial velocity (m)
$St$	Strouhal number
$S$	swirl number
$T_{ad}$	adiabatic flame temperature (K)
$T_{fl}$	flame temperature (K)
$T_{in}$	combustor inlet temperature (K)
$T^*$	normalized temperature
$u_0$	combustor inlet bulk velocity (m/s)
$(u, v, w)$	axial, radial, and tangential velocities (m/s)
$w_{H2}$	mass fraction of hydrogen
$X = (x, y, z)$	Cartesian coordinates (m)
$x_{fl}$	axial location of the CoG of the heat release (m)
$\phi$	equivalence ratio
$\Omega$	degree of humidity
$\Phi_j$	spatial POD mode
$\alpha_x$	local jet opening angle (rad)
$\alpha$	jet opening angle (rad)

## REFERENCES

- Acharya, V.S., Shin, D.-H., and Lieuwen, T. 2013. Premixed flames excited by helical disturbances: Flame wrinkling and heat release oscillations. *J. Propul. Power*, **29**, 1282–1291. DOI:10.2514/1.B34883
- Albin, E., Nawroth, H., Göke, S., D'Angelo, Y., and Paschereit, C.O. 2013. Experimental investigation of burning velocities of ultra-wet methane–air–steam mixtures. *Fuel Process. Technol.*, **107**, 27–35. DOI:10.1016/j.fuproc.2012.06.027
- Anacleto, P.M., Fernandes, E.C., Heitor, M.V., and Shtork, S.I. 2003. Swirl flow structure and flame characteristics in a model lean premixed combustor. *Combust. Sci. Technol.*, **175**, 1369–1388. DOI:10.1080/00102200302354
- Babkin, V., and V'yun, A. 1971. Effect of water vapor on the normal burning velocity of a methane–air mixture at high pressures. *Combust. Explos. Shockwaves*, **7**(3), 339–341.

- Bartlett, M.A., and Westermarck, M.O. 2005a. A study of humidified gas turbines for short-term realization in midsized power generation—Part II: Intercooled cycle analysis and final economic evaluation. *J. Eng. Gas Turbines Power*, **127**, 100–108. DOI:10.1115/1.1788684
- Bartlett, M.A., and Westermarck, M.O. 2005b. A study of humidified gas turbines for short-term realization in midsized power generation—Part I: Nonintercooled cycle analysis. *J. Eng. Gas Turbines Power*, **127**, 91–99. DOI:10.1115/1.1788683
- Berkooz, G., Holmes, P., and Lumley, J.L. 1993. The proper orthogonal decomposition in the analysis of turbulent flows. *Annu. Rev. Fluid Mech.*, **25**, 539–575. DOI:10.1146/annurev.fl.25.010193.002543
- Bhargava, A., Colket, M., Sowa, W.A., et al. 2000. An experimental and modeling study of humid air premixed flames. *J. Eng. Gas Turbines Power*, **122**, 405. DOI:10.1115/1.1286921
- Boxx, I., Arndt, C.M., Carter, C.D., and Meier, W. 2010. High-speed laser diagnostics for the study of flame dynamics in a lean premixed gas turbine model combustor. *Exp. Fluids*, **52**, 555–567. DOI:10.1007/s00348-010-1022-x
- Durox, D., Schuller, T., Noiray, N., and Candel, S. 2009. Experimental analysis of nonlinear flame transfer functions for different flame geometries. *Proc. Combust. Inst.*, **32**, 1391–1398. DOI:10.1016/j.proci.2008.06.204
- Findeisen, J., Gnirß, M., Damaschke, N., et al. 2005. 2D-Concentration measurements based on Mie scattering using a commercial PIV system. Presented at the 6th International Symposium Particle Image Velocimetry, Pasadena, CA, September 21–23.
- Freund, O., Schaefer, P., Rehder, H.-J., and Roehle, I. 2011. Experimental investigations on cooling air ejection at a straight turbine cascade using PIV and QLS. Presented at the ASME Turbo Expo, Vancouver, Canada, June 6–10.
- Froud, D., O'Doherty, T., and Syred, N. 1995. Phase averaging of the precessing vortex core in a swirl burner under piloted and premixed combustion conditions. *Combust. Flame*, **100**, 407–412.
- Gallaire, F., and Chomaz, J.-M. 2003. Mode selection in swirling jet experiments: A linear stability analysis. *J. Fluid Mech.*, **494**, 223–253. DOI:10.1017/S0022112003006104
- Gallaire, F., Ruith, M.R., Meiburg, E., et al. 2006. Spiral vortex breakdown as a global mode. *J. Fluid Mech.*, **549**, 71–90. DOI:10.1017/S0022112005007834
- Galley, D., Ducruix, S., Lacas, F., and Veynante, D. 2011. Mixing and stabilization study of a partially premixed swirling flame using laser induced fluorescence. *Combust. Flame*, **158**, 155–171. DOI:10.1016/j.combustflame.2010.08.004
- Galmiche, B., Halter, F., Foucher, F., and Dagaut, P. 2011. Effects of dilution on laminar burning velocity of premixed methane/air flames. *Energy Fuels*, **25**, 948–954.
- Giaque, A., Selle, L., Gicquel, L., et al. 2005. System identification of a large-scale swirled partially premixed combustor using LES and measurements. *J. Turbul.*, **6**, N21. DOI:10.1080/14685240512331391985
- Göckeler, K., Terhaar, S., and Paschereit, C.O. 2013. Residence time distribution in a swirling flow at non-reacting, reacting, and steam-diluted conditions. *J. Eng. Gas Turbines Power*, **136**(4), 041505.
- Göke, S., Göckeler, K., Krüger, O., and Paschereit, C.O. 2010. Computational and experimental study of premixed combustion at ultra wet conditions. Presented at the ASME Turbo Expo, Glasgow, Scotland, June 14–18.
- Göke, S., and Paschereit, C.O. 2013. Influence of steam dilution on nitrogen oxide formation in premixed methane/hydrogen flames. *J. Propul. Power*, **29**, 249–260. DOI:10.2514/1.B34577
- Hermeth, S., Staffelbach, G.M., Gicquel, L.Y., and Poinot, T. 2013. Bistable flame stabilization in swirled flames and influence on flame transfer functions. *Combust. Flame*, **161**, 184–196.
- Higgins, B., McQuay, M.Q., Lacas, F., et al. 2001. Systematic measurements of OH chemiluminescence for fuel—Lean, high-pressure, premixed, laminar flames. *Fuel*, **80**, 67–74. DOI:10.1016/S0016-2361(00)00069-7
- Huang, Y., and Yang, V. 2009. Dynamics and stability of lean-premixed swirl-stabilized combustion. *Prog. Energy Combust. Sci.*, **35**, 293–364.



- Huerre, P., and Monkewitz, P.A. 1990. Local and global instabilities in spatially developing fluids. *Annu. Rev. Fluid Mech.*, **22**, 473–537.
- Koroll, G.W., and Mulpuru, S.R. 1988. The effect of dilution with steam on the burning velocity and structure of premixed hydrogen flames. *Symp. (Int.) Combust.*, **21**(1), 1811–1819.
- Kuenne, G., Ketelheun, A., and Janicka, J. 2011. LES modeling of premixed combustion using a thickened flame approach coupled with FGM tabulated chemistry. *Combust. Flame*, **158**, 1750–1767. DOI:10.1016/j.combustflame.2011.01.005
- Leuckel, W. 1967. Swirl intensities, swirl types and energy losses of different swirl generating devices. IFRF Doc. Nr. G, 2:1–53.
- Liang, H., and Maxworthy, T. 2005. An experimental investigation of swirling jets. *J. Fluid Mech.*, **525**, 115–159. DOI:10.1017/S0022112004002629
- Lieuwen, T., and Yang, V. 2005. *Combustion Instabilities in Gas Turbine Engines: Operational Experience, Fundamental Mechanisms, and Modeling*, American Institute of Aeronautics and Astronautics, Reston, Virginia.
- Mazas, A.N., Fiorina, B., Lacoste, D.A., and Schuller, T. 2011. Effects of water vapor addition on the laminar burning velocity of oxygen-enriched methane flames. *Combust. Flame*, **158**, 2428–2440. DOI:10.1016/j.combustflame.2011.05.014
- Michalke, A. 1965. On spatially growing disturbances in an inviscid shear layer. *J. Fluid Mech.*, **23**, 521–544. DOI:10.1017/S0022112065001520
- Moeck, J.P., Bourgouin, J.-F., Durox, D., et al. 2012. Nonlinear interaction between a precessing vortex core and acoustic oscillations in a turbulent swirling flame. *Combust. Flame*, **159**, 2650–2668. DOI:10.1016/j.combustflame.2012.04.002
- Monkewitz, P.A., and Sohn, K. 1988. Absolute instability in hot jets. *AIAA J.*, **26**, 911–916. DOI:10.2514/3.9990
- Oberleithner, K., Paschereit, C.O., Seele, R., and Wygnanski, I. 2012. Formation of turbulent vortex breakdown: Intermittency, criticality, and global instability. *AIAA J.*, **50**, 1437–1452. DOI: 10.2514/1.J050642
- Oberleithner, K., Sieber, M., Nayeri, C.N., et al. 2011. Three-dimensional coherent structures in a swirling jet undergoing vortex breakdown: Stability analysis and empirical mode construction. *J. Fluid Mech.*, **679**, 383–414. DOI:10.1017/jfm.2011.141
- Oberleithner, K., Terhaar, S., Rukes, L., and Paschereit, C.O. 2013. Why non-uniform density suppresses the precessing vortex core. *J. Eng. Gas Turbines Power*, **135**(12), 121506.
- Roehle, I., Schodl, R., Voigt, P., and Willert, C.E. 2000. Recent developments and applications of quantitative laser light sheet measuring techniques in turbomachinery components. *Meas. Sci. Technol.*, **11**, 1023–1035. DOI:10.1088/0957-0233/11/7/317
- Roux, S., Lartigue, G., Poinsot, T., et al. 2005. Studies of mean and unsteady flow in a swirled combustor using experiments, acoustic analysis, and large eddy simulations. *Combust. Flame*, **141**, 40–54. DOI:10.1016/j.combustflame.2004.12.007
- Ruith, M.R., Chen, P., Meiburg, E., and Maxworthy, T. 2003. Three-dimensional vortex breakdown in swirling jets and wakes: Direct numerical simulation. *J. Fluid Mech.*, **486**, 331–378. DOI:10.1017/S0022112003004749
- Smith, G.P., Golden, D.M., Frenklach, M., et al. 2000. GRI-Mech 3.0.
- Stöhr, M., Sadanandan, R., and Meier, W. 2011. Phase-resolved characterization of vortex–flame interaction in a turbulent swirl flame. *Exp. Fluids*, **51**, 1153–1167. DOI:10.1007/s00348-011-1134-y
- Syred, N. 2006. A review of oscillation mechanisms and the role of the precessing vortex core (PVC) in swirl combustion systems. *Prog. Energy Combust. Sci.*, **32**, 93–161. DOI:10.1016/j.pecs.2005.10.002
- Syred, N., and Beér, J.M. 1974. Combustion in swirling flows: A review. *Combust. Flame*, **23**, 143–201.

- Terhaar, S., Bobusch, B.C., and Paschereit, C.O. 2012. Effects of outlet boundary conditions on the reacting flow field in a swirl-stabilized burner at dry and humid conditions. *J. Eng. Gas Turbines Power*. DOI:10.1115/1.4007165
- Terhaar, S., and Paschereit, C.O. 2012. High-speed PIV investigation of coherent structures in a swirl-stabilized combustor operating at dry and steam-diluted conditions. Presented at the 16th International Symposium on Applied Laser Technology to Fluid Mechanics, Lisbon, Portugal, July 9–12.
- Thumuluru, S.K., and Lieuwen, T. 2009. Characterization of acoustically forced swirl flame dynamics. *Proc. Combust. Inst.*, **32**, 2893–2900. DOI:10.1016/j.proci.2008.05.037
- Voigt, P., Schodl, R., and Griebel, P. 1997. Using the laser light sheet technique in combustion research. Proc. 90th Symp. AGARD-PEP Adv. Non-intrusive Instrum. Propuls. Engines.